https://doi.org/10.5194/egusphere-2025-6536
Preprint. Discussion started: 14 January 2026

Weekly-scale shoreline monitoring using low-cost UAV photogrammetry: A case study from a highly dynamic beach in Sri Lanka

Pituwala Liyanage Menusha Hasaranga[1], Thanthrige Windika Sameeth Warnasuriya[1], Nambukara Palliyaguruge Pushpitha[1]

[1]Department of Fisheries and Marine sciences, Ocean University, Tangalle, 82200, Sri Lanka

Correspondence to: P.L.M Hasaranga (Hasaranga099@gmail.com)

Abstract. Coastal areas worldwide are experiencing rapid changes due to erosion and sediment movement, yet monitoring these changes frequently remains economically challenging, especially in developing countries. This study presents an affordable approach to track shoreline changes over short time periods using widely available UAV (Unmanned Aerial Vehicle) technology and smartphone-based positioning systems. We monitored Red Beach in Sri Lanka weekly for one month, conducting aerial surveys at both high and low tides to capture how the beach changed day-to-day and throughout tidal cycles. The analysis performed using the digital shoreline analysis system in ArcGIS environment. Our findings revealed that the beach behaves as a complex, compartmentalized system where different sections respond differently to coastal processes. Although the beach showed overall sand accumulation during the study period, statistical analysis confirmed this growth occurred only in specific areas while other sections remained stable. The maximum zone of active change extended well beyond measurement uncertainties, indicating genuine coastal dynamics. Comparing high and low tide shorelines also revealed rapid, short-term shifts in active swash zone. This research demonstrates that affordable UAV-based mapping can effectively detect meaningful coastal changes, offering a practical solution for coastal management in regions with limited financial resources. Future work should explore integrating more accurate positioning devices at reasonable costs and extending monitoring over longer periods to capture seasonal patterns of erosion and accretion.

1 Introduction

Coastal morphology undergoes rapid changes characterized by complex geomorphological features influenced by both natural forces and anthropogenic activities. Consequently, regular monitoring of coastal morphology is essential to understand the nuanced patterns of environmental change (Jeong et al., 2018). Comprehending the complex dynamics of these ecosystems is critical for implementing effective coastal management strategies and adapting to ongoing environmental transformations. Short term coastal studies provide valuable insights into rapid changes occurring over short time scales, including shoreline displacement, erosion patterns, and habitat dynamics. Monitoring coastal processes at weekly scales enables researchers to assess the impacts of extreme events such as storms (Cowell and Thom, 1994), predict future coastal

https://doi.org/10.5194/egusphere-2025-6536
Preprint. Discussion started: 14 January 2026

changes, and develop informed management and planning strategies. Furthermore, these studies enhance our understanding of climate change impacts on coastal regions, enabling the development of adaptation and mitigation strategies to protect coastal ecosystems, communities, and infrastructure. However, the implementation of comprehensive high frequency monitoring programs is often hindered by significant financial and technical constraints, particularly in developing nations and resource-limited research settings (Wagener, 2005). Despite extensive research on coastal geomorphology addressing various aspects of coastal dynamics, significant gaps persist in shoreline definition, identification, interpretation, extraction, analysis, accuracy assessment, and the integration of volumetric analysis through continuous monitoring (Warnasuriya et al., 2022). Traditional beach survey methodologies employing high-precision instrumentation require substantial financial investments alongside considerable human resource commitments (Fang et al., 2021). This economic barrier is particularly problematic in resource-constrained regions experiencing extreme coastal conditions, where immediate and precise detection of subtle morphological changes is critical for risk assessment and management decisions (DahdouhGuebas et al., 2006). Consequently, there is an urgent need for cost-effective alternatives that maintain acceptable accuracy while reducing the economic burden of coastal monitoring.

Satellite-based remote sensing has emerged as one approach to reduce field survey costs while providing historical data and extensive spatial coverage, including access to remote or inaccessible areas (Papakonstantinou et al., 2017). However, its application for weekly-scale analysis is severely constrained by inherent limitations, including low temporal resolution, relatively coarse spatial resolution, and substantial acquisition costs for high-resolution commercial imagery (Ruiz-Beltran et al., 2019). These constraints impede the analysis of subtle morphological variations over short time frames, particularly at localized scales where erosion hotspots may span only tens of meters. Recent technological advancements have significantly improved the accessibility of Unmanned Aerial Vehicle (UAV) photogrammetry, with consumer-grade platforms now widely available and operational costs substantially lower than traditional surveying methods (Barbosa et al., 2024). Numerous studies have demonstrated that UAV photogrammetry achieves accuracy comparable to conventional techniques, including Real-Time Kinematic (RTK) and Differential Global Positioning System (DGPS) systems (Brasington et al., 2000; Squarzoni et al., 2005), total stations (Fuller et al., 2003; Moss et al., 1999), Terrestrial Laser Scanning (TLS) (Brasington et al., 2012a; Fairley et al., 2016), and Aerial Laser Scanning (ALS) requiring specialized aircraft and equipment (Dewitte et al., 2008 ; Notebaert et al., 2009). The development of affordable, lightweight UAV platforms, combined with rapid advancements in open-source computational algorithms such as Structure-from-Motion (SfM), has established UAVs as cost-effective technological alternatives for geomorphological research. UAV-based photogrammetry facilitates high-resolution topographic data acquisition at a fraction of traditional costs, enabling comprehensive spatial analyses previously accessible only to well-funded research programs (Colomina and Molina, 2014). Compared to conventional methodologies, UAVs offer substantial economic advantages while maintaining operational flexibility, rapid deployment capability, and the acquisition of imagery at very high spatial and temporal resolutions using consumer-grade cameras (Chen et al., 2018).

https://doi.org/10.5194/egusphere-2025-6536
Preprint. Discussion started: 14 January 2026

While UAV technology substantially reduces aerial data acquisition costs, ground control requirements have traditionally necessitated expensive high-precision positioning equipment. Contemporary GPS technologies such as RTK and DGPS systems remain the standard for ground control point (GCP) establishment in photogrammetric surveys (Stott et al., 2020). However, the substantial acquisition and maintenance costs of these sophisticated instruments frequently impose prohibitive financial constraints on research activities, particularly for long-term monitoring programs requiring repeated measurements (Gonçalves and Henriques, 2015). Furthermore, these systems often require specialized training and technical expertise, adding to the overall resource requirements. To address these limitations and enhance the economic feasibility of high frequency coastal monitoring, cost-effective positioning alternatives that balance ease of deployment with acceptable survey accuracy are critically needed.

High-sensitivity GPS chipsets have become widely integrated into consumer mobile devices in recent years and have demonstrated reliable performance under challenging environmental conditions (MacGougan et al., 2002; Watson, 2005). Modern smartphones integrate high-sensitivity GPS hardware with Assisted GPS (A-GPS) capabilities, enabling positioning in challenging environments (Lee et al., 2016). The positioning performance of mobile phones is comparable to standard consumer-grade GPS receivers, with testing across various environmental conditions indicating that significant positioning errors occur infrequently (Zandbergen and Barbeau, 2011). The integration of these readily accessible, low-cost positioning solutions with UAV photogrammetry presents a potentially viable approach for substantially reducing the overall economic burden of weekly-scale coastal monitoring while maintaining data quality suitable for scientific investigation and management applications.

This pilot study addresses the critical need for cost-effective methodologies to assess weekly-scale coastal dynamics, a research gap that has particularly limited monitoring capabilities in developing regions and resource-constrained institutional settings. The primary objectives are to: (1) demonstrate a low-cost workflow integrating consumer-grade UAVs and mobile phone GPS for weekly-scale coastal assessment (2) quantify coastal dynamics over short time periods using UAV-derived data (3) identify and characterize erosion and accretion hotspots along the coastline. By establishing the feasibility and accuracy thresholds of this low-cost approach, this research aims to enhance the accessibility of high-resolution weekly-scale coastal monitoring, enabling broader implementation of evidence-based coastal management strategies in economically constrained regions while contributing to our comprehensive understanding of rapid coastal morphological change.

https://doi.org/10.5194/egusphere-2025-6536
Preprint. Discussion started: 14 January 2026

2 Methodology

2.1. Study area

This study was conducted at Red Beach (6.015835° N, 80.786970° E), a prominent coastal tourist destination located in the Hambantota District along the southern coast of Sri Lanka (Fig. 1). The beach extends approximately 500 m in length and exhibits a curved morphology characteristic of pocket beaches. The coastal area demonstrates highly dynamic behavior, with continuous morphological changes driven by energetic wave conditions and seasonal variations. The site experiences significant wave action, with wave heights ranging from 0.6 m to 3.5 m **(**Survey Department of Sri Lanka, 2007). Tidal variation ranges between 0.4 m and 0.6 m (Morris, 1985)., while seasonal sea level fluctuations vary from 0.2 m to 0.3 m (Wijeratne, 2003). These energetic oceanographic conditions create a dynamic coastal environment subject to rapid morphological change, making it an ideal location for high frequecny monitoring studies. Tourism patterns at Red Beach exhibit strong seasonal variation, with peak visitation occurring from December to April. The energetic wave conditions make the beach less attractive to local visitors; however, international tourists frequently visit during the peak season to engage in beach-related leisure activities. To mitigate ongoing coastal erosion, the Coast Conservation Department has installed coastal protection structures, including a groyne and revetment system. Red Beach derives its name from the distinctive red coloration of its sand, which comprises a high concentration of garnet minerals, representing a unique geological feature along Sri Lanka's southern coast. The sediment composition includes traces of black ilmenite sand interspersed with white sand containing quartz (SiO_2) and calcium carbonate ($CaCO_3$) (Warnasuriya et al., 2025). The presence of economically valuable heavy minerals, particularly garnet and ilmenite, has implications for potential resource extraction industries. However, the area's primary economic value currently stems from its tourism potential, with the unique sand composition and coastal setting serving as major attractions.

https://doi.org/10.5194/egusphere-2025-6536
Preprint. Discussion started: 14 January 2026

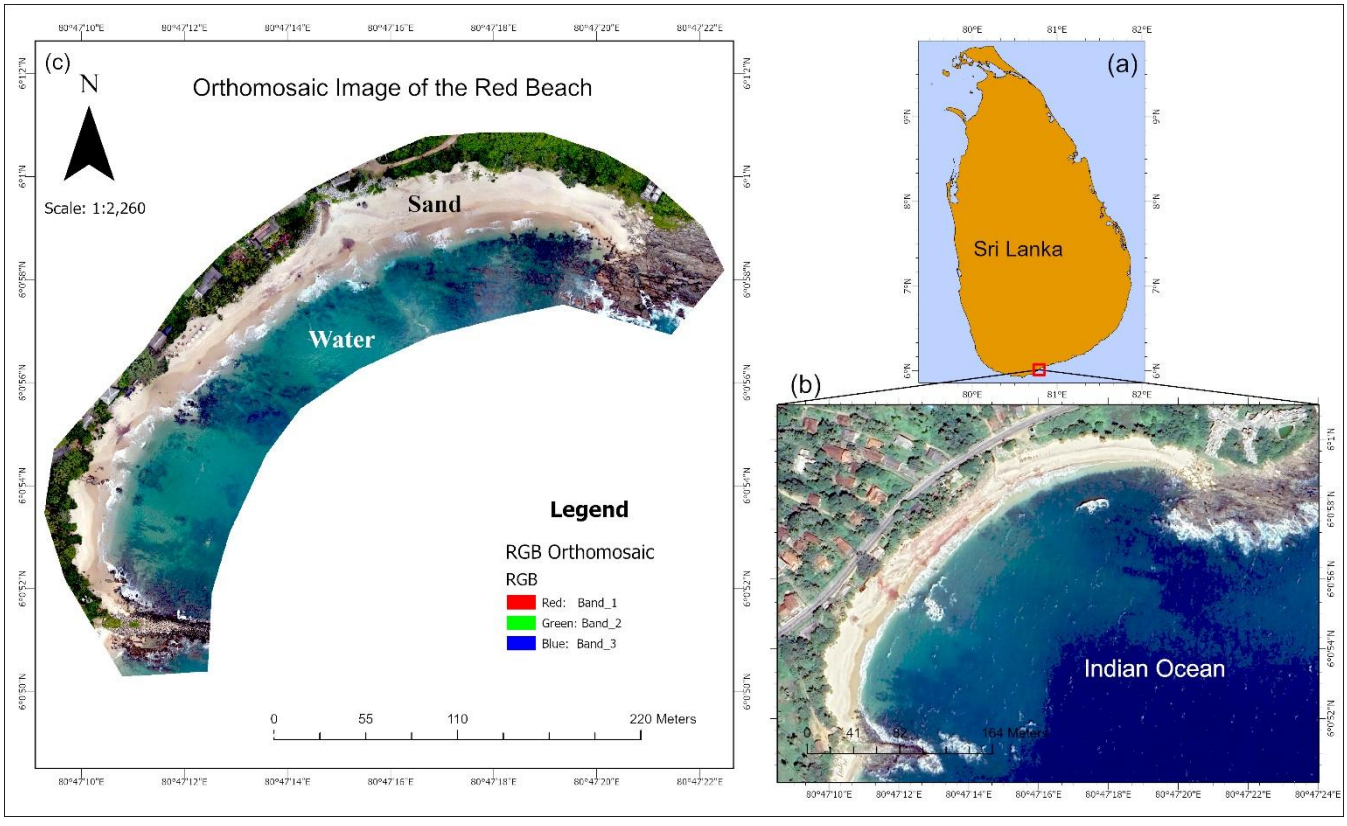

Figure 1(a) Study area in the south coast of Sri Lanka (red box), (b) aerial image of the Red beach (Imagery © 2025 Landsat/Copernicus, Map data © 2025 Google) and (c) high resolution orthomosaic image of the Red beach.

2.2 UAV remote sensing system

A DJI Mavic Air, a consumer-grade quadrotor UAV system manufactured by DJI (Shenzhen, China), was used to acquire aerial imagery of the study area (Fig. 2). The quadrotor platform was selected due to its vertical takeoff and landing capabilities, minimal spatial requirements for deployment, and portability, making it well-suited for coastal environments with limited access. The UAV system consisted of an unmanned aircraft, remote controller, three intelligent flight batteries with charging station, and a 4K camera. The camera was mounted on the front of the aircraft and stabilized using a three-axis gimbal. The system integrated multiple sensors including GPS, GLONASS, inertial measurement unit, barometer, and compass, enabling autonomous flight capabilities (Support for Mavic Air – DJI , 2025).

The UAV supported hovering, GPS position hold, and autopilot navigation along predetermined flight paths programmed in the flight plan. The system achieved a maximum cruising speed of 19 m/s and was powered by lithium-polymer batteries. Each battery provided approximately 21 minutes of flight time under standard conditions. Flight operations were limited to a maximum duration of 18 minutes per battery as a safety precaution, particularly under moderate wind conditions and high

https://doi.org/10.5194/egusphere-2025-6536
Preprint. Discussion started: 14 January 2026

temperatures. For larger survey areas requiring extended flight time, multiple flights with battery replacements were necessary (Mohsan et al., 2022). The UAV was rated for operation in wind speeds up to 10 m/s; however, flights were conducted only when wind speeds were below 10 m/s to ensure flight stability and image quality while minimizing coverage gaps. The remote controller, connected to a mobile device via Wi-Fi and radio linkage enabled real-time monitoring of flight parameters and captured imagery. The main technical specifications of the UAV system are presented in Table 1.

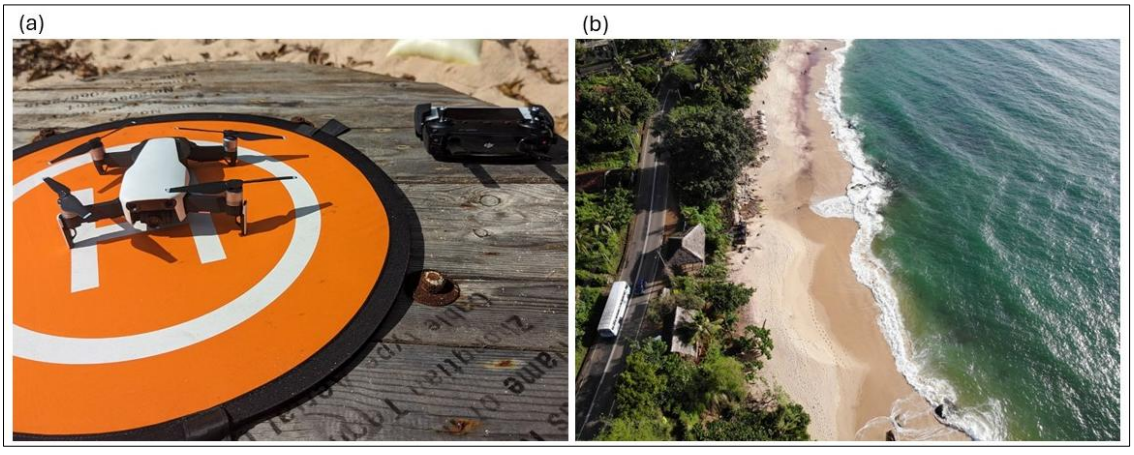

Figure 2 (a) DJI Mavic Air UAV System and remote controller used for aerial image acquisition. (b)Aerial image captured from DJI Mavic Air UAV at 60 m altitude. This platform was selected for its portability and capacity to capture high-resolution imagery for subsequent photogrammetric processing and analysis.

Table 1 Main specifications of the Mavic Air UAV system.

Feature	Value
Camera Sensor	1/2.3” CMOS (Effective Pixels: 12 MP)
Takeoff Weight	430 g
Dimensions Unfolded	168×184×64 mm (L×W×H)
Max Speed (near sea level, no wind)	19 ms^{-1}
Max Ascent Speed	4 ms^{-1}
Max Flight Time (No wind)	21 min
Max Flight Distance (no wind)	10 km

https://doi.org/10.5194/egusphere-2025-6536
Preprint. Discussion started: 14 January 2026

2.3 Data collection

2.3.1 Acquisition of aerial images

Prior to UAV flight operations, a preliminary field investigation was conducted to assess beach topographic features, identify important infrastructure, and detect potential sources of electromagnetic interference that could affect GPS and compass functionality. Flight planning and parameter configuration were performed using the DroneDeploy version 5.40 (DroneDeploy, Inc.,2023) application, which determined the flight path, altitude, speed, and image overlap specifications (Table 2). To investigate weekly-scale coastal dynamics at Red Beach, aerial surveys were conducted on four separate days in December 2023 within the Northeast Monsoon. Flights were executed during both morning and evening periods each day to capture morphological changes across different tidal phases (Table 3). Given the beach's relatively small dimensions (average width of approximately 15 m), a single flight pattern was sufficient to cover the entire monitoring area during each survey. However, battery replacement was required mid-flight to complete the full coverage. The DroneDeploy application facilitated this process by enabling mission pause during battery exchanges, allowing seamless continuation of the flight plan.

Survey dates were selected through a coordinated planning process to ensure compliance with both meteorological safety standards and national aviation regulations. Since Unmanned Aerial Vehicle (UAV) operations in Sri Lanka require prior security clearance and approval from the Civil Aviation Authority (CAA) and the Ministry of Defence (MOD) specifying exact dates and locations, flight schedules had to be determined in advance. Consequently, dates were selected by consulting forecasts from the Department of Meteorology (2023) to target specific windows of stable atmospheric conditions, which were then submitted for regulatory approval to secure the necessary flight permissions. Prior to each data acquisition session, Ground Control Points (GCPs) were established and surveyed. Flight operations were then conducted, and GCP coordinates were recorded using mobile phone GPS receivers. Each survey session yielded approximately 200 overlapping aerial images of Red Beach. The resulting imagery clearly resolved typical coastal features, including the shoreline, vegetation cover, and sand surface, with a ground sampling distance of approximately 2 cm throughout the study period.

https://doi.org/10.5194/egusphere-2025-6536
Preprint. Discussion started: 14 January 2026

Table 2 Main flight parameters for the UAV flight operation.

Parameter	Value
Camera angle	70°
Flight altitude	60 m
Front overlap	75 %
Side overlap	70 %
Flight speed	5 ms^{-1}
Flight Pattern	Double grid

Table 3 Aerial survey dates and corresponding tidal conditions (Source: Galle tide station, Sri Lanka)

Date	Tide Phase	Tide Value (m)
2023/12/08	Low tide	0.49
	High tide	0.57
2023/12/12	Low tide	0.31
	High tide	0.68
2023/12/20	Low tide	0.39
	High tide	0.60
2023/12/27	Low tide	0.31
	High tide	0.71

https://doi.org/10.5194/egusphere-2025-6536
Preprint. Discussion started: 14 January 2026

2.3.2 Ground control point distribution

Ground Control Points (GCPs) are essential for producing geometrically accurate orthomosaic products. At Red Beach, the surface was predominantly covered by sand and sparse vegetation, which did not provide easily identifiable natural features suitable for use as GCPs. Consequently, artificial markers were deployed throughout the monitoring area. Due to the energetic wave conditions and persistent wind at the beach, a total of 20 high-density polystyrene signboards (12 × 12 × 3 cm) (Fig. 3) were installed as GCP markers. GPS coordinates for each GCP were acquired using the Polaris Navigation GPS version 9.25 (DS Software , 2023) mobile application, which provided an estimated horizontal accuracy of 2 m.

Concurrently, reference photographs of each GCP and its surrounding environment were captured to facilitate accurate marker identification and placement during the subsequent image orientation process. To assess the absolute planimetric accuracy of the orthomosaics generated for each survey period, permanent structures including buildings, embankments, and large rocks were selected as independent Check Points (CPs). These CPs were also surveyed using the Polaris Navigation GPS mobile application with an estimated horizontal accuracy of 2 m.

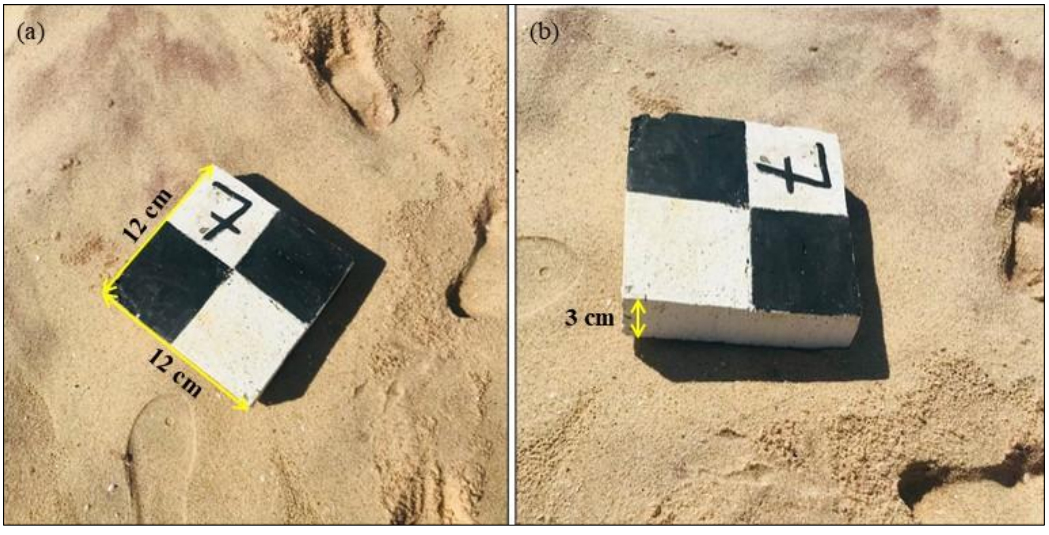

Figure 3 Example of a Ground Control Point (GCP) marker used for image georeferencing. The marker is made from polystyrene and has dimensions of 12 cm x 12 cm x 3 cm (a) Top-down view showing the 12cm x 12cm top surface. The checkerboard pattern and unique identification number (7) are designed for high visibility and accurate detection during image processing and photogrammetric workflows. (b) Side view illustrating the 3 cm thickness of the marker.

https://doi.org/10.5194/egusphere-2025-6536
Preprint. Discussion started: 14 January 2026

2.3.4 Orthomosaic model generation

Orthomosaic generation from UAV imagery requires specialized photogrammetric software. Several commercial and open-source software packages based on Structure-from-Motion (SfM) algorithms have been developed specifically for UAV image processing. The SfM algorithm enables the reconstruction of accurate orthomosaics and three-dimensional models from overlapping photographs captured at various viewing angles (Lowe et al., 2019). For this study, Agisoft Metashape Professional Free trial version 2.0.3 (Agisoft LLC, 2023) software was selected based on its user-friendly interface, comprehensive analytical capabilities, and optimization for UAV-derived imagery, factors that have contributed to its widespread adoption in aerial imagery applications (Kostrzewa et al., 2025). The general processing workflow is illustrated in Figure 4.

In the preprocessing stage, all UAV imagery was imported into Agisoft Metashape Professional software. Images were manually inspected and excluded if they were captured before takeoff, after landing, or exhibited excessive blur or distortion. The project coordinate system was configured to WGS 84 (EPSG:4326) to match the coordinate reference system of the GPS-derived GCPs. Image alignment was performed using the software's automated photo alignment tool with the following parameters: alignment quality set to high accuracy, generic and reference preselection enabled, key point limit set to 40,000, tie point limit set to 4,000, and adaptive camera model fitting activated.

This initial alignment produced a sparse three-dimensional point cloud representing the scene geometry based on conjugate feature points extracted from overlapping images. Following initial alignment, GCP coordinates were imported into the reference pane. Horizontal coordinates (longitude and latitude) were obtained from the Polaris Navigation mobile application, while vertical coordinates (elevation) were extracted from the UAV image metadata. Each GCP marker was manually identified and linked across 10-12 images to ensure robust spatial referencing. The sparse point cloud was then systematically refined using the gradual selection tool to remove points with high reprojection error and reconstruction uncertainty. Additional outliers were identified through visual inspection and manually removed. Camera alignment was subsequently optimized using all available camera calibration parameters (f, b_1, b_2, cx, cy, k_1-k_3, p_1, p_2) to minimize geometric distortions. After optimization, dense point clouds were generated using multi-view stereo reconstruction. From the dense point clouds, georeferenced orthomosaic imagery models were produced for each survey period. The final planimetric accuracy of these products was confirmed in the subsequent accuracy assessment (Section 3.1). Figure 5 presents a time-series montage of the generated orthomosaics, visually demonstrating the high spatial resolution and the temporal coverage of the study area across the four-week survey period, captured at both high and low tide stages. These products provided the foundation for subsequent shoreline extraction.

https://doi.org/10.5194/egusphere-2025-6536
Preprint. Discussion started: 14 January 2026

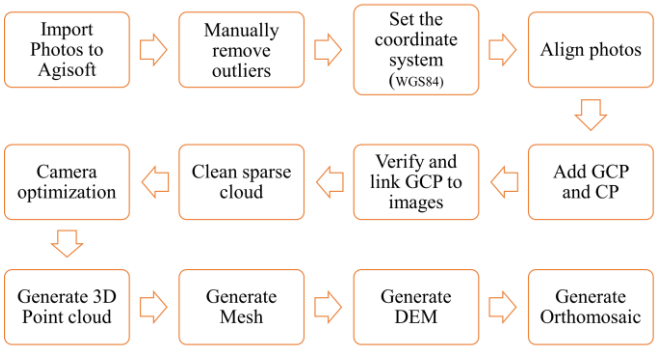

Figure 4 Photogrammetric workflow implemented for processing the Unmanned Aerial Vehicle (UAV) imagery using Agisoft Metashape Professional 2.0.3.

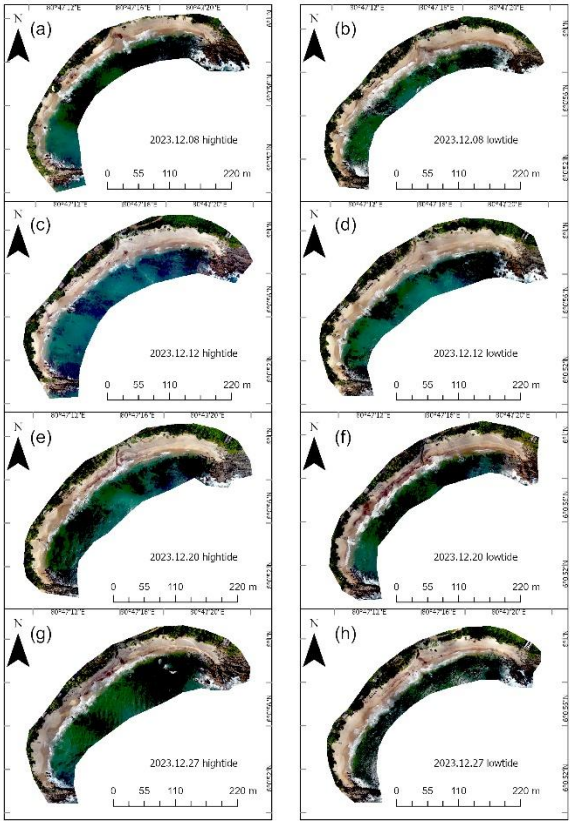

Figure 5 Time-series of orthomosaics from weekly UAV surveys capturing tidal-phase shoreline variations. Eight panels represent the study area at high tide (HT) and low tide (LT) on four survey dates during December 2023: (a) 08 Dec HT, (b) 08 Dec LT, (c) 12 Dec HT, (d) 12 Dec LT, (e) 20 Dec HT, (f) 20 Dec LT, (g) 27 Dec HT, (h) 27 Dec LT. Orthomosaics provided the base layer for dry-wet line proxy digitization and subsequent shoreline change analysis.

https://doi.org/10.5194/egusphere-2025-6536
Preprint. Discussion started: 14 January 2026

2.3.5 Accuracy assessment

The planimetric accuracy of orthomosaics was assessed using a dual methodology appropriate for low-cost change detection studies (James and Robson, 2014). Two accuracy metrics serve distinct purposes: relative accuracy quantifies the consistency of measurements between survey epochs (critical for change detection), while absolute accuracy indicates positional fidelity relative to global coordinate systems. Relative accuracy was calculated using the Root Mean Square Error ($RMSE_{xy}$) of Ground Control Points (GCPs) used in the photogrammetric bundle block adjustment. This metric reflects the internal geometric consistency of each orthomosaic and represents the precision with which shoreline positions can be compared between survey dates (Sohl and Mahmood, 2024). GCP RMSE values ranged from 0.51m to 1.53m across the eight surveys, with a mean of 1.095m. This relative accuracy is sufficient for detecting shoreline changes exceeding the calculated uncertainty threshold of ±2.36m (Section 2.3.7) Absolute accuracy was assessed using independent Check Points (CPs) excluded from model generation. These points, located on permanent features (buildings, large rocks, embankment corners), were surveyed with the same smartphone GPS used for GCPs and compared against their positions in the orthomosaics. CP RMSE values ranged from 2.27m to 4.85m, with a mean of 4.019m. The comparatively high absolute error reflects the cumulative influence of three factors: (1) the inherent ±2m horizontal accuracy limitation of consumer smartphone GPS receivers, (2) checkpoint feature identification uncertainty when matching field GPS positions to corresponding locations in sub-decimeter resolution orthomosaics (estimated at 1.0-1.5m based on repeated identification tests), and (3) potential GPS multipath effects, which may vary between GCP locations (open beach) and CP locations (near structures). To investigate this, we compared CP errors for points located in open areas (mean RMSE = 2.9m) versus points adjacent to buildings or vegetation (mean RMSE = 4.8m), confirming that multipath contributed approximately 2m additional error at structurally complex locations.

2.3.6 Extraction of shoreline and geomorphological metrics

All spatial data extraction and processing were conducted using ArcGIS 10.5 (Esri, 2017) software. Shorelines were extracted from the high-resolution orthomosaic images using manual digitization at a scale of 1:500. The Dry-Wet Line (DWL) was selected as the shoreline indicator due to its clear visibility in the imagery and widespread use in coastal studies (Boak and Turner, 2005). All digitized shorelines were saved in shapefile (.shp) format. The shoreline change analysis was initially conducted on the full, unsegmented shoreline to generate the whole beach statistics reported in the results (Section 3.2). Due to the high dynamism of the beach and spatial variability in geomorphological features, the study area was segmented into three distinct sections (Left, Mid, and Right) based on two prominent geomorphological discontinuities. (Fig. 6) This segmentation was subsequently used for both the advanced statistical analysis (Section 2.5) and the extraction of secondary geomorphological metrics. Beach surface area was delineated using manual digitization techniques applied to each orthomosaic image at a scale of 1:600. Manual digitization was chosen over automated classification to maximize local accuracy and ensure the reliable delineation of complex and spectrally heterogeneous beach features. These varying scales

https://doi.org/10.5194/egusphere-2025-6536
Preprint. Discussion started: 14 January 2026

285 were selected to optimize visual identification for each feature while maintaining overall digitization efficiency. All delineated polygons were saved in shapefile (.shp) format. Beach width was measured using the Multipoint tool in conjunction with the Measure tool in ArcGIS. Points were placed along the landward baseline and the high-water line, and perpendicular distances between corresponding points were measured to determine beach width at regular intervals along the coast.

290

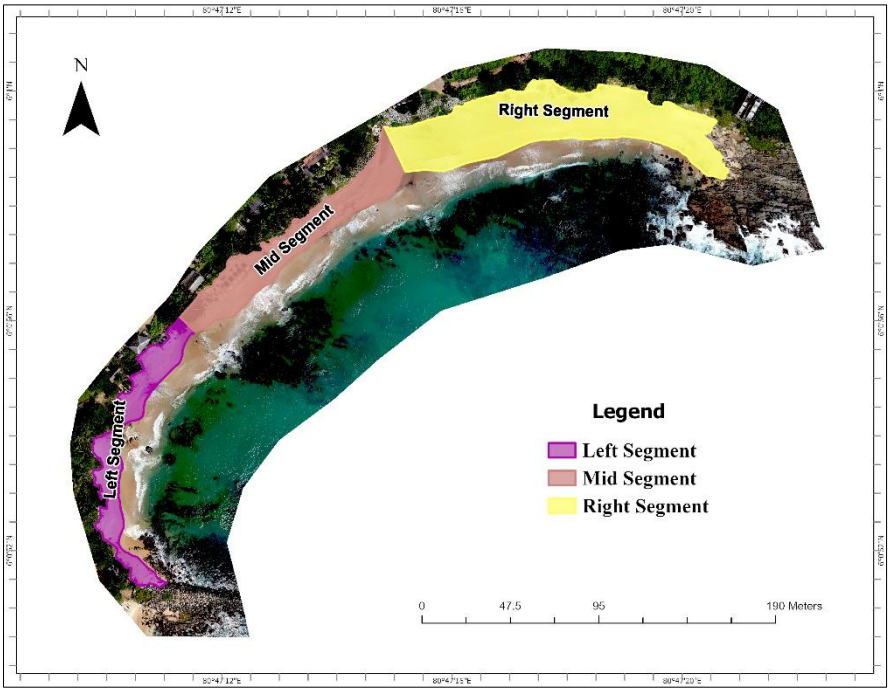

Figure 6 Spatial segmentation of the beach based on geomorphological characteristics. The study area was divided into three segments (left, middle, right) delineated by two prominent geomorphological discontinuities caused by drainage outlets.

2.3.7 Uncertainty estimation

295 Shoreline positional uncertainty (U_p) was quantified for each digitized shoreline to establish a statistically defensible threshold for distinguishing actual coastal change from measurement error. The total positional uncertainty was calculated using the root sum of squares of four component errors.

$$U_P = \sqrt{E_{rect}^2 + E_{tidal}^2 + E_{pixel}^2 + E_{digit}^2} \quad (1)$$

300

E_{rect} represents georeferencing error, E_{tidal} represents horizontal error resulting from water level fluctuations, E_{digit} represents manual digitization error, and E_{pixel} represents image resolution error. The georeferencing uncertainty (E_{rect}) was derived

https://doi.org/10.5194/egusphere-2025-6536
Preprint. Discussion started: 14 January 2026

from the Ground Control Point (GCP) RMSE rather than the checkpoint (CP) RMSE. GCP RMSE represents the relative accuracy between successive surveys, which is more appropriate for change detection studies than absolute positional accuracy. This approach maintains sensitivity to weekly morphological changes while accepting higher absolute positional error, a compromise consistent with the low-cost monitoring framework. The mean georeferencing uncertainty was 1.095 m. Tidal uncertainty (E_{tidal}) was calculated by projecting the estimated vertical uncertainty in tidal prediction (E_v = 0.1m) onto the horizontal plane using the mean beach slope (θ = 8.18°) reported by Warnasuriya (2025).

$$E_{tidal} = \frac{E_v}{\tan(\theta)} \quad (2)$$

The pixel resolution error (E_{pixel}) was set to 0.02 m based on ground sampling distance. Manual digitization uncertainty (E_{digit}) was estimated at 1.0 m based on repeated digitization tests of the same shoreline. The calculated average positional uncertainty for a single shoreline was U_p = ±1.67 m. For shoreline change analysis between any two survey dates, the combined uncertainty (U_{total}) was calculated as: Eq. (3)

$$U_{total} = \sqrt{U_{p,t1}^2 + U_{p,t2}^2} \quad (3)$$

resulting in a mean detection threshold of ±2.36 m. Only Net Shoreline Movement (NSM) values exceeding this threshold were considered statistically significant indicators of coastal change.

2.4 Data analysis

2.4.1 Shoreline change analysis

Shoreline shapefiles were imported into ArcGIS 10.5 and organized into separate datasets according to tidal phase (high tide and low tide). The merged shoreline datasets were stored in a personal geodatabase and projected to the WGS 84 UTM Zone 44N coordinate system to ensure spatial consistency. Date and uncertainty attributes were added to the attribute table of each shoreline dataset. Date attributes recorded the acquisition time of each shoreline position, while uncertainty values quantified the positional accuracy of shoreline delineation. A reference baseline was manually created landward of all shoreline positions for each tidal dataset to serve as the origin for transect-based measurements. Each baseline was assigned a unique identifier in its attribute table. Approximately 100 Shore-perpendicular transects were generated at 5 m intervals along each baseline using the Digital Shoreline Analysis System (DSAS) add-in developed by the United States Geological Survey (USGS) for use within the ESRI ArcGIS environment. (Himmelstoss et al., 2021). The transect search distance was set to 100 m to ensure intersection with all shoreline positions, and a smoothing distance of 10 m was applied to reduce local

https://doi.org/10.5194/egusphere-2025-6536
Preprint. Discussion started: 14 January 2026

variability in transect orientation (Fig. 7). These parameters were selected based on the beach dimensions and orientation variability.

Shoreline change statistics were calculated using DSAS 5.0 at a 95% confidence interval for both high tide and low tide scenarios. The following metrics were computed: Shoreline Change Envelope (SCE), which measures the maximum range of shoreline movement; Net Shoreline Movement (NSM), which quantifies the distance between the oldest and most recent shoreline positions; End Point Rate (EPR), which calculates the rate of change between the oldest and most recent shorelines. Supplementary statistics including the coefficient of determination (WR^2) and descriptive statistics (mean and standard deviation) were computed for each metric to characterize the central tendency and variability of shoreline change along the coast.

To assess inter-tidal zone variations induced by tidal oscillations, shoreline positions were extracted at both high-tide and low-tide phases on each survey date. Since DSAS requires a unique date attribute for each shoreline feature to execute statistical calculations, and both tidal phases occurred on the same calendar day, a methodological workaround was implemented. Low-tide shorelines were assigned their actual survey dates, while high-tide shorelines were assigned mock dates corresponding to the day following the survey date (e.g., if the survey was conducted on December 15, the low-tide shoreline was dated December 15 and the high-tide shoreline was dated December 16). This approach allowed DSAS to process the dataset without temporal conflicts while maintaining the sequential relationship between tidal phases. Since DSAS requires unique dates for each shoreline and both tidal phases occurred on the same calendar day, rate-based metrics (EPR, LRR) could not be calculated for the tidal analysis. Instead, we focus on distance-based metrics (SCE and NSM) which accurately quantify the spatial separation between high-tide and low-tide shorelines on each survey date.

https://doi.org/10.5194/egusphere-2025-6536
Preprint. Discussion started: 14 January 2026

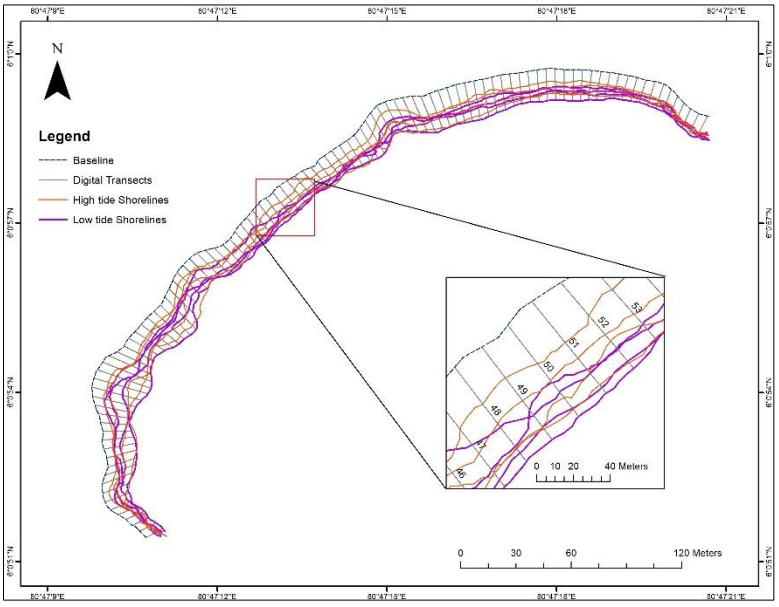

Figure 7 Digital Shoreline Analysis System (DSAS) setup for shoreline change assessment. The baseline (dashed line) and shore-perpendicular transects intersect high-tide shorelines and low-tide shorelines extracted from eight survey dates. Inset panel provides magnified view of transect spacing and tidal-phase shoreline positions.

2.4.2 Statistical analysis

One-way Analysis of Variance (ANOVA) was performed to test for significant differences in shoreline change statistics among the three beach segments. This analysis was conducted separately for high tide and low tide datasets to assess whether geomorphological segmentation captured meaningful spatial variation in coastal dynamics. Beach width data were analyzed using Repeated Measures ANOVA in IBM SPSS Statistics 25 (IBM Corporation, 2017) software to evaluate temporal changes in beach dimensions across the study period. Descriptive statistics were calculated to characterize the magnitude and variability of beach width changes. Beach surface area was analyzed using SPSS software. One-way ANOVA tests were performed to assess significant differences in these parameters among beach segments. Descriptive statistics were calculated to summarize the spatial and temporal patterns of the beach area changes.

3 Results

3.1 Shoreline change by whole beach

Analysis of digital transects across the entire beach revealed substantial shoreline mobility during the study period (Fig. 8, Table 4). The grand mean (mean ± SD) Shoreline Change Envelope (SCE) was 8.385 ± 3.79 m, indicating considerable spatial variability in shoreline position. Net Shoreline Movement (NSM) averaged 4.94 ± 5.47 m across all transects and

https://doi.org/10.5194/egusphere-2025-6536
Preprint. Discussion started: 14 January 2026

mean End Point Rate was 7.905 m ± 8.77 m /month (Fig. 9). Weighted linear regression (WLR) analysis yielded an R^2 value of 0.468, indicating no consistent directional trend in shoreline displacement. This lack of a clear temporal pattern likely reflects the combined influences of wave runup, backwash, tidal oscillations, and short-term erosion-accretion cycles that obscured longer-term shoreline behavior.

Table 4 Overall shoreline change statistics for the entire study area. Values represent means calculated from digital transects across the whole beach during the monitoring period.

Shoreline Indicator	Tide Phase	SCE (m) (mean ± SD)	NSM (m) (mean ± SD)	EPR (m/month) (mean ± SD)	WR^2 (mean ± SD)
DWL	Low tide	7.87 ± 3.68	4.77 ± 5.60	7.63 ± 8.97	0.43 ± 0.33
DWL	Hight tide	8.90 ± 3.90	5.10 ± 5.35	8.18 ± 8.57	0.50 ± 0.35

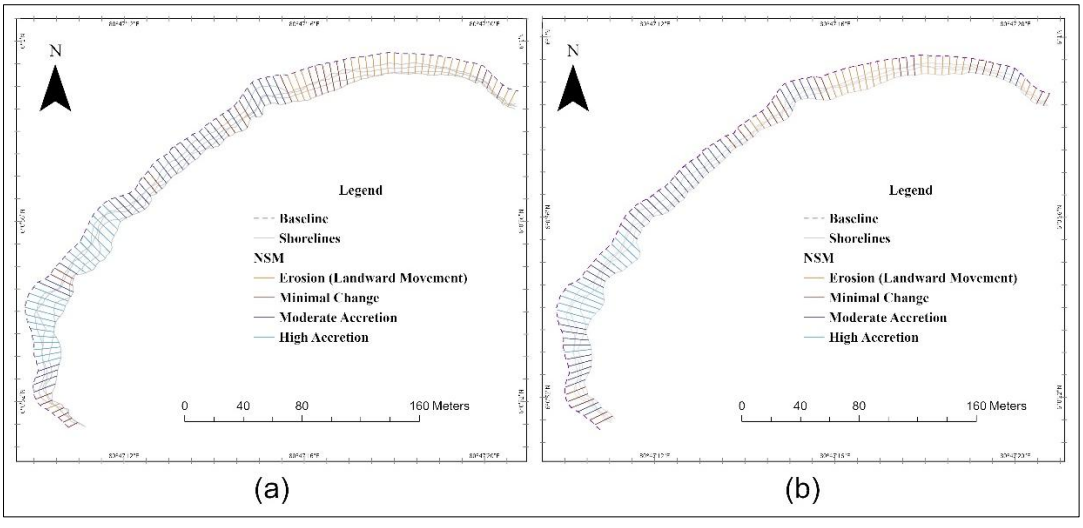

Figure 8 Spatial distribution of Net Shoreline Movement (NSM) for (a) low-tide shoreline and (b) high-tide shoreline during the monitoring period. Transects indicate areas of erosion (landward movement) and accretion (seaward movement).

https://doi.org/10.5194/egusphere-2025-6536
Preprint. Discussion started: 14 January 2026

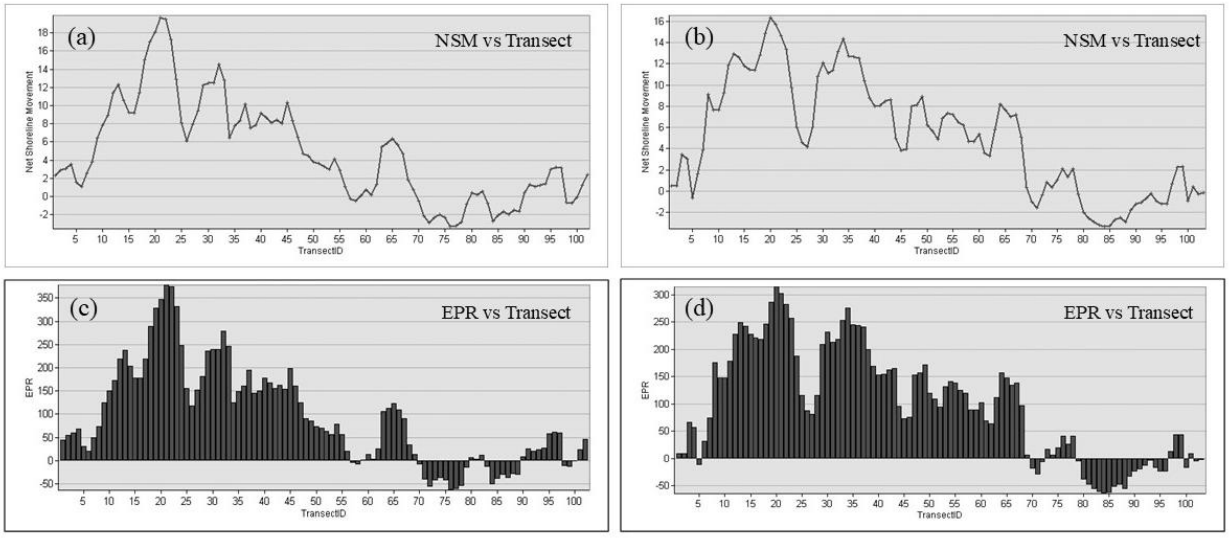

Figure 9 Shoreline change analysis showing Net Shoreline Movement (NSM) and End Point Rate (EPR) along numbered digital transects for the study period. (a) NSM vs Transect derived from the Low Tide Shoreline positions, indicating the total measured change in meters. (b) NSM vs Transect derived from the High Tide Shoreline positions, indicating the total measured change in meters. (c) EPR vs Transect derived from the Low Tide Shoreline positions, illustrating the annualized rate of change m/ year (d) EPR vs Transect derived from the High Tide Shoreline positions, illustrating the annualized rate of change m/year.

3.2 Shoreline change by beach segment

Spatial analysis revealed significant variability in shoreline dynamics between beach segments for both Shoreline Change Envelope (SCE) and Net Shoreline Movement (NSM) metrics (Table 5). One-way ANOVA tests indicated significant differences between segments for all metrics and tidal phases ($p < 0.05$). The left segment consistently demonstrated the highest variability and accretion magnitude, with mean NSM values exceeding 9 m during both tidal phases—approximately four times greater than the total uncertainty threshold (U_{total} = ±2.36 m). The middle segment exhibited moderate accretion (4.70 to 6.40 m), while the right segment remained in near-equilibrium, with mean NSM values (−0.14 to 0.07 m) falling within measurement uncertainty. Post-hoc Tukey pairwise comparisons revealed significant differences ($p < 0.05$) between the left segment and both other segments for all metrics. During high tide conditions, significant differences also emerged between the middle and right segments for SCE values, indicating enhanced spatial variability under elevated water levels. This pronounced spatial gradient demonstrates that beach-averaged NSM values (approximately 5.0 m) were disproportionately influenced by extreme accretion in the left segment, suggesting differential exposure to wave energy and variations in sediment supply across the study area.

https://doi.org/10.5194/egusphere-2025-6536
Preprint. Discussion started: 14 January 2026

Table 5 Summary statistics for shoreline change metrics across beach segments

Metric (m)	Tidal Phase	Left segment (mean ± SD)	Mid segment (mean ± SD)	Right segment (mean ± SD)	ANOVA
SCE	Low tide	10.57 ± 4.21	6.14 ± 2.29	6.46 ± 2.12	$p < 0.05$
SCE	High tide	11.03 ± 4.59	8.88 ± 1.85	6.85 ± 3.20	$p < 0.05$
NSM	Low tide	9.64 ± 5.12	4.70 ± 3.31	0.07 ± 2.46	$p < 0.05$
NSM	High tide	9.38 ± 4.74	6.40 ± 1.76	−0.14 ± 2.53	$p < 0.05$

3.3 Inter-tidal zone width variability

The horizontal separation between high-tide and low-tide shoreline positions quantifies the width of the active inter-tidal zone on each survey date (Table 6, Figure 10). Net Shoreline Movement (NSM) between tidal phases averaged -1.88 ± 2.34 m across all surveys, with considerable week-to-week variability. The negative sign indicates landward positioning of the high-tide shoreline relative to the low-tide shoreline, as expected on a sloping beach.

Week 2 (December 12) exhibited the largest inter-tidal separation (NSM = -4.15 ± 2.34 m), exceeding the combined uncertainty threshold (U_{total} = ±2.36 m) and indicating a statistically significant wide inter-tidal zone. The Shoreline Change Envelope for this date (SCE = 4.18 ± 2.28 m) was nearly identical to the NSM, suggesting relatively uniform cross-shore separation along the beach length. In contrast, Week 3 (December 20) showed minimal separation (NSM = 1.45 ± 2.38 m) that was not statistically significant, with the smallest SCE value (1.98 m) observed during the study period. Weeks 1 and 4 exhibited intermediate values (NSM = -2.52 and -2.17 m respectively).

The substantial variability in inter-tidal zone width (ranging from 1.45 to 4.15 m between weeks) demonstrates that the horizontal extent of the active swash zone fluctuates on weekly timescales. While the grand mean NSM (-1.88 m) across all surveys is not statistically significant, the grand mean SCE (2.84 m) confirms a real zone of tidal influence exists. This week-to-week variation likely reflects changes in beach profile shape in response to varying wave conditions, though actual elevation data would be required to confirm this interpretation.

https://doi.org/10.5194/egusphere-2025-6536
Preprint. Discussion started: 14 January 2026

Table 6 Inter-tidal zone metrics quantifying horizontal separation between low-tide and high-tide shoreline positions for each survey date. NSM indicates mean cross-shore distance; SCE indicates maximum observed separation. Negative NSM values indicate landward high-tide position.

Shoreline Indicator	Week	SCE (m) (mean ± SD)	NSM (m) (mean ± SD)
DWL	1	2.56 ± 2.06	-2.52 ± 2.11
DWL	2	4.18 ± 2.28	-4.15 ± 2.34
DWL	3	1.98 ± 1.95	1.45 ± 2.38
DWL	4	2.48 ± 1.25	-2.17 ± 1.74

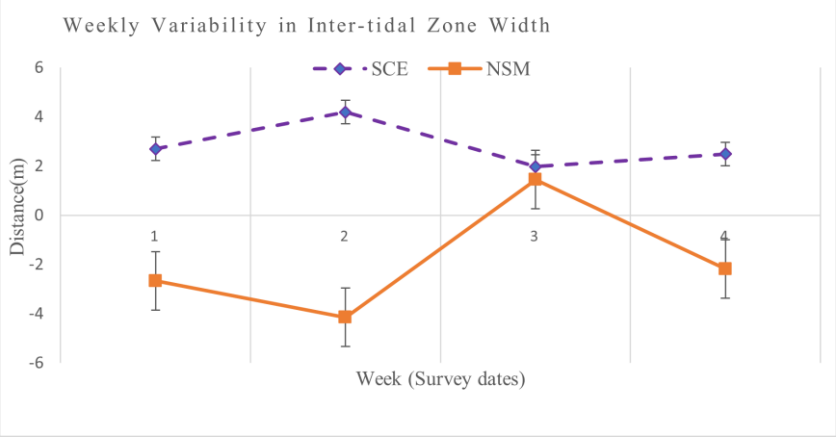

Figure 10 Weekly variability in inter-tidal zone width. Shoreline Change Envelope (SCE) represents the maximum observed horizontal separation between high-tide and low-tide shoreline positions, while Net Shoreline Movement (NSM) represents the mean cross-shore distance (negative values indicate landward high-tide position) on each survey date.

3.4 Beach width

The results of the Repeated Measures ANOVA revealed significant main effects for both time and site ($p < 0.05$) on beach width (Fig.11). The interaction effect between time and site (Time x Site) was also significant ($p < 0.05$), indicating that temporal changes in beach width varied spatially across the study area. The grand mean (mean ± SD) of the beach width was

https://doi.org/10.5194/egusphere-2025-6536
Preprint. Discussion started: 14 January 2026

16.350 ± 0.643 m. Post hoc pair wise comparisons revealed that there were Significant mean differences of beach width between the right and mid segments ($p < 0.05$), as well as between the right and left segments ($p < 0.05$). However, there was no significant difference between the mid and left segment ($p > 0.05$). Right segment had the highest mean beach width (20.852 ± 2.40 m) followed by mid segment (15.364 ± 2.62 m) and left segment (12.834 ± 4.36 m). The significant time and site interaction indicates that the temporal variability of beach width was site-dependent, with different segments responding differently to the same temporal forcing factors.

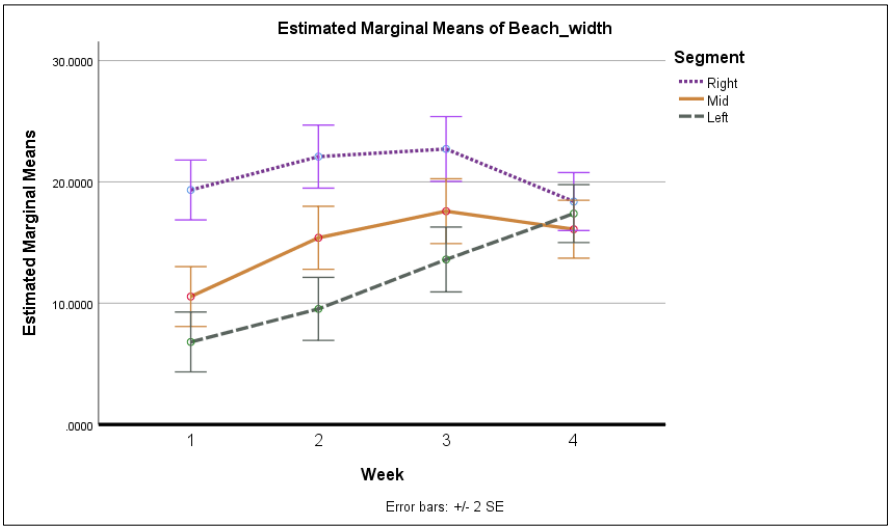

Figure 11 Beach width dynamics in different segments throughout the study period. Temporal trends show distinct patterns of beach width variation among the left, middle, and right segments, reflecting differential responses to wave and tidal forcing.

3.5 Beach surface area

One-way ANOVA indicated significant differences in beach surface area among the three beach segments ($p < 0.05$). The right segment had the greatest mean surface area (4087.80 m²), accounting for approximately 50% of the total beach area, followed by the mid segment (2141.82 m², 26%) and the left segment (1908.94 m², 24%). Temporal analysis revealed contrasting trends among segments over the monitoring period. The right segment exhibited a slight decrease in surface area (−1.4%, from 3689.97 m² to 3639.96 m²), while both the mid and left segments showed substantial increases of 59.4% (from 1511.89 m² to 2409.85 m²) and 107.8% (from 1258.05 m² to 2614.44 m²), respectively (Fig. 10). Overall, total beach surface area increased significantly by 34.1% throughout the monitoring period, from 6459.91 m² to 8664.26 m².

https://doi.org/10.5194/egusphere-2025-6536
Preprint. Discussion started: 14 January 2026

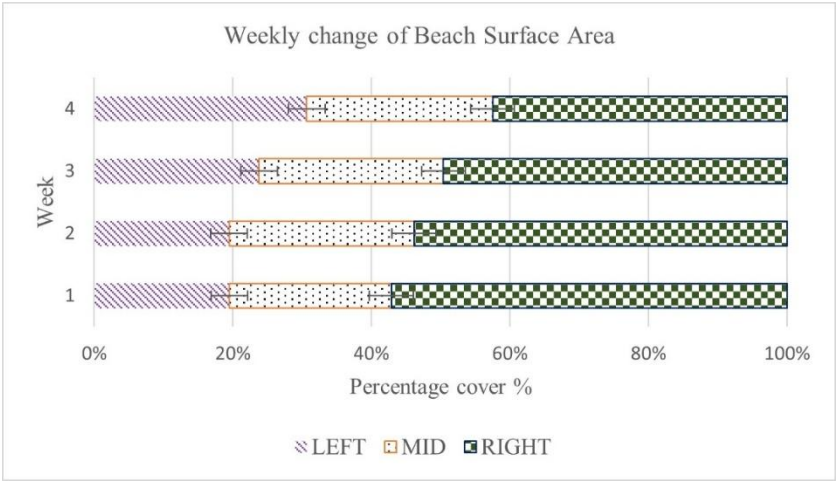

Figure 12 Temporal changes in proportional surface area of beach segments. Stacked bars show the percentage contribution of each segment (left, middle, right) to total beach area on each survey date.

4 Discussion

4.1 Efficacy of high-frequency monitoring and shoreline dynamics

The results of this study demonstrate that Red Beach acts as a highly dynamic geomorphological system characterized by significant, yet spatially non-uniform, morphological changes over weekly scales. The use of high-frequency UAV monitoring allowed for the capture of rapid coastal processes that are often smoothed over or missed by traditional seasonal or annual surveys (Turner et al., 2016). The most robust evidence of this morphological variability is the high magnitude of the Shoreline Change Envelope (SCE), which reached mean values of 7.87 m (Low Tide) and 8.90 m (High Tide). These values far exceed the calculated total uncertainty threshold (U_{total} = ± 2.36 m), confirming that the beach experienced substantial physical modification within the single-month study period. This finding is critical for coastal management in the region, as the SCE defines the maximum active zone, which serves as a more conservative and relevant metric for defining setback limits than the mean Net Shoreline Movement (NSM) in highly active environments. While the mean NSM values indicated a statistically significant net accretion trend (4.77 m for Low Tide and 5.11 m for Hight Tide), this overall average masked critical spatial variability. The initial observation of high Standard Deviation values relative to the mean (SD > Mean) suggested a heterogeneous response along the coast. This was statistically validated by the One-Way ANOVA, which confirmed a significant difference in mean shoreline change between the three geomorphological segments ($p < 0.05$).

The Tukey post-hoc analysis revealed that the beach operates as three distinct morphological compartments. The Left Segment was the primary driver of the observed whole-beach accretion, advancing seaward by over 9 m (Table 5), likely influenced by the groyne structure which traps sediment in this zone (Sujivakand et al., 2024). Groynes are designed to trap

https://doi.org/10.5194/egusphere-2025-6536
Preprint. Discussion started: 14 January 2026

longshore sediment transport, causing accretion updrift (in this case, the left segment) and potential erosion downdrift (Sujivakand et al., 2024). In contrast, the Right Segment remained statistically stable, with mean NSM values (0.07 m and -0.14 m) falling well within the ± 2.36 m uncertainty threshold. This segmentation analysis resolves the ambiguity of the high whole-beach variability, demonstrating that average shoreline change is an insufficient metric for Red Beach without spatial compartmentalization. The analysis of secondary geomorphological metrics (Beach Surface Area and Beach Width) further corroborates the spatial compartmentalization identified by the shoreline change statistics. The temporal increase in beach surface area observed in the Left and Mid segments aligns perfectly with the high positive NSM values recorded in these zones, confirming that the shoreline advancement represented substantial sediment gain rather than mere profile readjustment. Conversely, the stability or slight reduction in surface area in the Right segment mirrors its non-significant NSM results. This multidimensional coherence between linear (NSM) and areal (Surface Area) metrics validates the low-cost photogrammetry workflow's ability to capture complex morphological evolution beyond simple shoreline position.

Furthermore, the study highlights the non-linear and episodic nature of short-term coastal change. The extremely low determination coefficients (mean $WR^2 < 0.5$) obtained for the Weighted Linear Regression (WLR) indicate that the shoreline did not follow a consistent linear trend even over this short duration.

4.2 Inter-tidal zone dynamics and tidal uncertainty

The horizontal separation between high-tide and low-tide shorelines varied substantially between weeks (range: 1.45-4.15 m), indicating that the active inter-tidal zone width fluctuates on weekly timescales. Week 2 exhibited the widest zone (4.15 m, exceeding U_{total}), while Week 3 showed minimal separation (1.98 m, within uncertainty). These variations likely reflect changes in beach face slope responding to varying wave conditions, though elevation data would be required for definitive interpretation.

This analysis validates the tidal uncertainty component (E_{tidal} = 0.695 m) in our positional uncertainty budget, which represents 29% of total single-shoreline uncertainty (U_p = 1.67 m). The documented tidal-phase variability confirms that accounting for water level differences is essential when comparing shorelines extracted at different tidal stages.

4.2 Methodological feasibility and accuracy considerations

This study addresses the critical need for low-cost, accessible monitoring solutions in resource-constrained developing regions. The workflow successfully demonstrates that consumer-grade UAVs combined with mobile-GPS ground control can generate data suitable for identifying statistically significant coastal changes, provided that the uncertainty is rigorously quantified. A primary technical limitation identified is the high Absolute Accuracy error, quantified by the mean independent Check Point (CP) RMSE of 4.019 m. This error, driven by the 2 m accuracy of the mobile phone GPS used for ground control, precludes the use of these orthomosaics for applications requiring high-precision absolute geodetic positioning.

https://doi.org/10.5194/egusphere-2025-6536
Preprint. Discussion started: 14 January 2026

However, the methodology's strength lies in its Relative Accuracy (mean GCP RMSE of 1.095 m). Since the internal geometry of the models is consistent, relative changes between shorelines could be detected with a calculated confidence threshold of ± 2.36 m. This approach allowed the study to differentiate effectively between measurement noise (observed in the Right Segment) and real morphological change (observed in the Left Segment). This trade-off accepting lower absolute accuracy to achieve high-frequency temporal resolution at a fraction of the cost of RTK/DGPS surveys is justified for rapid assessment and disaster risk management in coastal areas where expensive equipment is unavailable.

4.3 Limitations

Important limitations must be acknowledged. The one-month monitoring period captured only a snapshot of beach behavior during a single season (Northeast Monsoon). The net accretion observed may represent normal seasonal variability rather than sustained trends. The high Absolute Accuracy (mean CP RMSE of 4.019 m) limitation does not invalidate change detection analyses, as these rely on relative accuracy between co-registered datasets. However, it does constrain certain applications: (1) integration with high-precision geodetic networks, (2) precise volumetric calculations requiring accurate elevation data, and (3) direct comparison with satellite imagery or government cadastral surveys without co-registration. For applications requiring absolute positioning better than 2-3m, professional RTK-GNSS ground control would be necessary. This accuracy trade-off is inherent to the low-cost monitoring approach and represents a deliberate methodological choice, accepting lower absolute accuracy in exchange for dramatically increased monitoring frequency and spatial coverage. For coastal management applications focused on detecting morphological change trends (erosion/accretion patterns, storm impacts, seasonal variability), relative accuracy is the critical metric, and the demonstrated ±2.36m detection threshold is appropriate for monthly-scale beach dynamics in high-energy environments where typical changes exceed 5-10m annually. Another limitation is the reliance on the Dry-Wet Line (DWL) as the shoreline indicator. Although clearly identifiable in the imagery, the DWL's positional accuracy is inherently influenced by factors not fully controlled, such as moisture content, sediment color, and wave run-up at the time of flight (Boak and Turner, 2005). This introduces variability that is contained within the ± 2.36 m uncertainty budget but represents a source of measurement noise.

4.3 Recommendations for future research

The study period was constrained by logistical challenges and unfavorable weather conditions in the study area. Future investigations should extend monitoring duration to several months or longer to identify temporal trends and seasonal patterns in beach morphology. Volumetric analysis should be incorporated to quantify three-dimensional sediment budget changes and identify additional coastal dynamics such as beach profile evolution and slope variations (Zanutta et al., 2020) . Further studies integrating advanced UAV photogrammetry systems with high-accuracy positioning instruments would help refine this methodology and establish optimal equipment configurations for various coastal settings. Additionally, comparative studies across beaches with different geomorphological characteristics, exposure conditions, and sediment

https://doi.org/10.5194/egusphere-2025-6536
Preprint. Discussion started: 14 January 2026

compositions would enhance understanding of the methodology's applicability and limitations in diverse coastal environments.

5 Conclusion

This study demonstrated that Red Beach functions as a highly dynamic, spatially compartmentalized geomorphological system. Weekly monitoring over one month (December 2023) revealed that shoreline changes are driven by rapid, episodic events rather than linear trends, with significant spatial variability necessitating a segmented analytical approach. Key findings indicate that whole-beach statistics can obscure critical localized processes. While the overall beach exhibited net accretion, one-way ANOVA confirmed that this pattern was driven primarily by the left segment, whereas the right segment remained in dynamic equilibrium. Furthermore, the Shoreline Change Envelope (SCE) emerged as the most critical metric for coastal management, defining a maximum active zone (mean > 7 m) that substantially exceeded net shoreline movement. The intra-day analysis further highlighted the system's volatility, capturing rapid transformations between dissipative and reflective beach profiles within single-week intervals. Methodologically, this research establishes a replicable framework for low-cost coastal monitoring in resource-constrained settings. The study confirmed that while consumer-grade UAVs combined with mobile phone GPS ground control exhibited limited absolute accuracy (checkpoint RMSE ≈ 4 m), they achieved sufficient relative accuracy (ground control point RMSE ≈ 1.1 m) to reliably detect morphological changes. By rigorously quantifying the total uncertainty budget (±2.36 m), including specific parameterization for tidal error, this workflow enables statistically valid identification of erosion and accretion events without expensive survey-grade GNSS equipment. This validation of consumer-grade technology demonstrates that high-temporal-resolution monitoring is achievable within the financial constraints typical of developing nations and under-resourced research institutions.

For coastal management at Red Beach specifically, our findings yield several actionable recommendations. (1) Groyne performance monitoring: The dramatic accretion in the left segment suggests the existing groyne is effectively trapping sediment, but this may be creating sediment starvation downdrift. Monthly monitoring using the demonstrated low-cost approach should continue to assess whether the right segment transitions from equilibrium to erosion, which would indicate adverse impacts requiring mitigation measures such as beach nourishment or groyne modification. (2) Setback zone delineation: The maximum SCE values define the active coastal zone where infrastructure placement should be avoided or specially designed. Current setback regulations should incorporate segment-specific risk zones rather than applying uniform distances, given the threefold difference in mobility between segments. (3) Tourism facility planning: The high weekly variability in beach width and profile indicates that beach accessibility and safety conditions can change rapidly. Tourism operators and local authorities should implement weekly beach profile assessments during peak season (December-April) to inform visitor safety advisories and facility placement.

https://doi.org/10.5194/egusphere-2025-6536
Preprint. Discussion started: 14 January 2026

(4) Early warning system development: The demonstrated workflow provides a foundation for rapid-response monitoring following extreme events. Post-storm surveys conducted within 24-48 hours using this approach (total survey time <6 hours, processing <8 hours) can quantify damage and inform emergency beach recovery priorities more cost-effectively than traditional surveying. (5) Regional replication: Similar compartmentalized behavior likely exists at other groyne-protected beaches along Sri Lanka's southern coast. The Coast Conservation Department should consider adapting this monitoring protocol for systematic assessment of coastal protection structure performance across multiple sites.

Beach environments exhibit non-linear morphological changes over short time scales, rendering traditional, infrequent surveys inadequate for capturing event-driven dynamics (Ciavola and Coco, 2017; Splinter et al., 2014). The high-frequency monitoring approach presented here detected changes that would have been completely missed by seasonal or annual surveys, particularly the rapid oscillations between erosional and accretional states within weekly intervals. This temporal resolution is critical for understanding process-response relationships in high-energy coastal environments and for implementing timely management interventions (Masselink et al., 2016). Consequently, this low-cost, high-frequency methodology warrants application to similar high-energy beaches globally, particularly in regions where conventional high-precision surveying remains economically prohibitive. The demonstrated accuracy thresholds and uncertainty quantification provide a basis for establishing minimum standards for cost-effective coastal monitoring programs. By making high-resolution morphological monitoring accessible to resource-limited settings, this approach enhances capacity for evidence-based coastal zone planning and disaster risk management in the communities most vulnerable to coastal change.

https://doi.org/10.5194/egusphere-2025-6536
Preprint. Discussion started: 14 January 2026

Code availability

The analysis presented in this paper relied on standard functions within commercial software. Agisoft Metashape Professional Free trial version 2.0.3 for orthomosaic generation; ESRI ArcGIS 10.5 and ArcGIS Pro 3.3.2 for shoreline change analysis (DSAS) and final map preparation and IBM SPSS Statistics 25 for statistical testing. No custom code was generated.

Data availability

Data availability. The shoreline shapefiles, DSAS transect statistics, beach morphology shapefiles and their measurements are available at https://doi.org/10.5281/zenodo.18082190 (Hasaranga et al., 2025). Orthomosaic images (1-2 GB per survey date) are available upon request from the corresponding author due to file size constraints.

Interactive computing environment

No interactive computing environment was used for this research.

Sample availability

No physical samples were collected or used in this study.

Video supplement

No video supplement was submitted with this manuscript.

https://doi.org/10.5194/egusphere-2025-6536
Preprint. Discussion started: 14 January 2026

Author contribution

Conceptualization, SW; methodology, SW and MH ; validation, SW and GP; formal analysis, MH; investigation, MH; resources, SW and GP; data curation, MH; writing and original draft preparation, MH; writing, reviewing and editing, SW,MH and GP; visualization, MH; supervision, SW and GP; project administration, SW; All authors have read and agreed to the published version of the manuscript.

Competing interests

The authors declare that they have no conflict of interest.

Disclaimer

No disclaimer is applicable to this research.

Acknowledgements

A preliminary version of this work was previously presented at the National Aquatic Resources Research and Development Agency (NARA) Scientific Sessions 2024. The abstract, titled 'Micro-temporal shoreline change assessment using UAV photogrammetry,' is published in the conference proceedings and is formally cited in the References section of this manuscript. The authors would like to express their sincere gratitude to the Ocean University of Sri Lanka for providing the necessary resources and facilities that made this research possible. All the people supported in data collection are also highly appreciated. We are deeply thankful to the Ministry of Defence and the Civil Aviation Authority of Sri Lanka for granting permission to conduct UAV operations in the study area. AI tools, including Gemini AI and Claude AI, were utilized solely for improving the grammar and enhancing the overall clarity of the English language text and played no role in the scientific content, data analysis, or interpretation.

Financial support

This research received no specific grant from any funding agency in the public, commercial, or not-for-profit sectors and was conducted as a self-funded study.

https://doi.org/10.5194/egusphere-2025-6536
Preprint. Discussion started: 14 January 2026

References

Agisoft LLC: Agisoft Metashape Professional (Version 2.0.3), Agisoft LLC, St. Petersburg, Russia, https://www.agisoft.com, 2023.

Barbosa , P. C., Fargas Jr., D. C., and Narciso, G. A. M.: Comparative Analysis of Low-cost Consumer Grade and Commercial Grade Drones For Land Surveying Applications, ISPRSArchives, XLVIII4/W82023, 31–37, https://doi.org/10.5194/isprsarchivesXLVIII4W82023312024, 2024.

Boak, E. H. and Turner, I. L.: Shoreline Definition and Detection: A Review, Journal of Coastal Research, 214, 688–703, https://doi.org/10.2112/03-0071.1, 2005.

Brasington, J., Rumsby, B., and Mcvey, R.: Monitoring and Modelling Morphological Change in a Braided GravelBed River Using High Resolution GPSBased Survey, Earth Surface Processes and Landforms, 25, 973–990, https://doi.org/10.1002/10969837(200008)25:9%3C973::AIDESP111%3E3.0.CO;2Y, 2000.

Brasington, J., Vericat, D., and Rychkov, I.: Modeling river bed morphology, roughness, and surface sedimentology using high resolution terrestrial laser scanning, Water Resources Research, 48, https://doi.org/10.1029/2012wr012223, 2012a.

Chen, B., Yang, Y., Wen, H., Ruan, H., Zhou, Z., Luo, K., and Zhong, F.: High-resolution monitoring of beach topography and its change using unmanned aerial vehicle imagery, Ocean & Coastal Management, 160, 103–116, https://doi.org/10.1016/j.ocecoaman.2018.04.007, 2018.

Ciavola, P. and Coco, G. (Eds.): Coastal storms: processes and impacts , John Wiley & Sons , Western Sussex , UK , 288pp., ISBN 9781118937105, 2017.

Colomina, I. and Molina, P.: Unmanned aerial systems for photogrammetry and remote sensing: A review, ISPRS Journal of Photogrammetry and Remote Sensing, 92, 79–97, https://doi.org/10.1016/j.isprsjprs.2014.02.013, 2014.

Cowell, P. J. and Thom, B. G.: Morphodynamics of coastal evolution, Coastal evolution: Late Quaternary shoreline morphodynamics, 33–86, 1994.

DahdouhGuebas, F., Verheyden, A., G, K. J., P, J. L., and Koedam, N.: Capacity building in tropical coastal resource monitoring in developing countries: A reappreciation of the oldest remote sensing method, International Journal of Sustainable Development & World Ecology, 13, 62–76, https://doi.org/10.1080/13504500609469662, 2006.

https://doi.org/10.5194/egusphere-2025-6536
Preprint. Discussion started: 14 January 2026

Department of Meteorology ,15 day forecast: https://meteo.gov.lk/, last access: 4 December 2023.

Dewitte, O., Jasselette, J. C., Cornet, Y., Den, V., Collignon, A., Poesen, J., and Demoulin, A.: Tracking landslide displacements by multitemporal DTMs: A combined aerial stereophotogrammetric and LIDAR approach in western Belgium, Engineering Geology, 99, 11–22, https://doi.org/10.1016/j.enggeo.2008.02.006, 2008.

DJI , Support for Mavic Air : https://www.dji.com/global/support/product/mavic-air, last access: 2 December 2025.

DroneDeploy , Inc.: DroneDeploy (version 5.40), DroneDeploy, Inc., San Francisco, CA, https://www.dronedeploy.com, 2023

DS Software: Polaris GPS Navigation (Version 9.25), Santa Fe New Mexico, https://play.google.com/store/apps/details?id=com.discipleskies.android.polarisnavigation, 2023.

Esri : ArcGIS Desktop (Version 10.5), Esri, Redlands, CA, https://www.esri.com, 2017.

Fairley, I., Thomas, T., Phillips, M., and Reeve, D.: Terrestrial Laser Scanner Techniques for Enhancement in Understanding of Coastal Environments, 273–289, https://doi.org/10.1007/9783319251219_11, 2016.

Fuller, I. C., Large, A. R., and Milan, D. J.: Quantifying channel development and sediment transfer following chute cutoff in a wandering gravelbed river, Geomorphology, 54, 307–323, 2003.

Gonçalves, J. A. and Henriques, R.: UAV photogrammetry for topographic monitoring of coastal areas, ISPRS Journal of Photogrammetry and Remote Sensing, 104, 101–111, https://doi.org/10.1016/j.isprsjprs.2015.02.009, 2015.

Hasaranga, M., Warnasuriya, T. W. S., and Pushpitha, N. P. G.: Micro-temporal shoreline change assessment using UAV photogrammetry, in: Proceedings, International Conference -NARA Scientific Sessions , Colombo, 2024.

Himmelstoss, E. A., Henderson, R. E., Kratzmann, M. G., and Farris, A. S.: Digital Shoreline Analysis System (DSAS) version 5.1 user guide, Open-File Report, https://doi.org/10.3133/ofr20211091, 2021.

IBM Corporation: IBM SPSS Statistics 25 , IBM Corporation, Armonk, NY, https://www.ibm.com/analytics/spss-statistics, 2017.

https://doi.org/10.5194/egusphere-2025-6536
Preprint. Discussion started: 14 January 2026

James, M. R. and Robson, S.: Mitigating systematic error in topographic models derived from UAV and ground-based image networks, Earth Surface Processes and Landforms, 39, 1413–1420, https://doi.org/10.1002/esp.3609, 2014.

Kostrzewa, A., PłatekŻak, A., Banat, P., and Wilk, Ł.: OpenSource vs. Commercial Photogrammetry: Comparing Accuracy and Efficiency of OpenDroneMap and Agisoft Metashape, ISPRSArchives, XLVIII1/W42025, 65–72, https://doi.org/10.5194/isprsarchivesXLVIII1W42025652025, 2025.

Lee, L., Jones, M., Ridenour, G. S., Bennett, S. J., Majors, A. C., Melito, B. L., and Wilson, M. J.: Comparison of Accuracy and Precision of GPS Enabled Mobile Devices, in: IEEE International Conference on Computer and Information Technology (CIT), 73–82, https://doi.org/10.1109/CIT.2016.94, 2016.

Lowe, M., Adnan, F., Hamylton, S., Carvalho, R., and Woodroffe, C.: Assessing Reef-Island Shoreline Change Using UAV-Derived Orthomosaics and Digital Surface Models, Drones, 3, 44, https://doi.org/10.3390/drones3020044, 2019.

MacGougan, G., Lachapelle, G., Klukas, R., Siu, K., Garin, L., Shewfelt, J., and Cox, G.: Performance analysis of a standalone highsensitivity receiver, GPS Solutions, 6, 179–195, 2002.

Masselink, G., Castelle, B., Scott, T., Dodet, G., Suanez, S., Jackson, D., and Floc'h, F.: Extreme wave activity during 2013/2014 winter and morphological impacts along the Atlantic coast of Europe, Geophysical Research Letters, 43, 2135–2143, 2016.

Mohsan, S. A. H., Khan, M. A., Noor, F., Ullah, I., and Alsharif, M. H.: Towards the Unmanned Aerial Vehicles (UAVs): A Comprehensive Review, Drones, 6, 147, https://doi.org/10.3390/drones6060147, 2022.

Morris , R. O.: Colombo to Sangama Kanda Point, No. 813, Crown, Taunton, 1985.

Moss, J. L., McGuire, W. J., and Page, D.: Ground deformation monitoring of a potential landslide at La Palma, Canary Islands, Journal of Volcanology and Geothermal Research, 94, 251–265, https://doi.org/10.1016/S03770273(99)001067, 1999.

Notebaert, B., Verstraeten, G., Govers, G., and Poesen, J.: Qualitative and quantitative applications of LiDAR imagery in fluvial geomorphology, Earth Surface Processes and Landforms, 34, 217–231, 2009.

Papakonstantinou, A., Doukari, M., and Topouzelis, K.: COASTLINE CHANGE DETECTION USING UNMANNED AERIAL VEHICLES AND IMAGE PROCESSING TECHNIQUES, Fresenius Environmental Bulletin, 26, 5564–5571, 2017.

https://doi.org/10.5194/egusphere-2025-6536
Preprint. Discussion started: 14 January 2026

Patricia, A., Moar, A., Salles, P., and Appendini, C.: ShortTerm Shoreline Trend Detection Patterns Using SPOT5 Image Fusion in the Northwest of Yucatan, Mexico, Estuaries and Coasts, 42, https://doi.org/10.1007/s12237019005737, 2019.

Sohl, M. A. and Mahmood, S. A.: Lowcost UAV in photogrammetric engineering and remote sensing: Georeferencing, DEM accuracy, and geospatial analysis, Journal of Geovisualization and Spatial Analysis, 8, 14, 2024.

Splinter, K. D., Turner, I. L., Davidson, M. A., Barnard, P., Castelle, B., and Oltman-Shay, J.: A generalized equilibrium model for predicting daily to interannual shoreline response, Journal of Geophysical Research: Earth Surface, 119, 1936–1958, 2014.

Squarzoni, C., Delacourt, C., and Allemand, P.: Differential singlefrequency GPS monitoring of the La Valette landslide (French Alps), Engineering Geology, 79, 215–229, https://doi.org/10.1016/j.enggeo.2005.01.015, 2005.

Stott, E., Williams, R. D., and Hoey, T. B.: Ground Control Point Distribution for Accurate KilometreScale Topographic Mapping Using an RTKGNSS Unmanned Aerial Vehicle and SfM Photogrammetry, Drones, 4, 55, https://doi.org/10.3390/drones4030055, 2020.

Sujivakand , J., Samarasekara , R. S. M., Siriwardana , H. P. A. M., Anthony , D. R., and Hasitha Siriwardana: Unmanned aerial vehicles (UAVs) for coastal protection assessment: A study of detached breakwater and groins at Marawila Beach, Sri Lanka, Regional studies in marine science, 69, 103282–103282, https://doi.org/10.1016/j.rsma.2023.103282, 2024.

Survey Department: The national atlas of Sri Lanka, 2nd ed., Survey Department of Sri Lanka , Colombo , ISBN 9789559059042, 2007.

Turner, I. L., Harley, M. D., and Drummond, C. D.: UAVs for coastal surveying, Coastal Engineering, 114, 19–24, https://doi.org/10.1016/j.coastaleng.2016.03.011, 2016.

Wagener, A. de L. R.: Constraints to the implementation of effective environmental management in coastal areas of developing countries, Anais da Academia Brasileira de Ciências, 77, 613–623, https://doi.org/10.1590/s0001-37652005000400004, 2005.

Watson, R., Lachapelle, G., Klukas, R., Turunen, S., Pietilä, S., and Halivaara, I.: Investigating GPS Signals Indoors with Extreme High-Sensitivity Detection Techniques, Navigation, 52, 199–213, https://doi.org/10.1002/j.2161-4296.2005.tb00363.x, 2005.

https://doi.org/10.5194/egusphere-2025-6536
Preprint. Discussion started: 14 January 2026

Wijeratne, E. M. S: Tidal Characteristics and Modelling of Tidal Wave Propagation in Shallow Lagoons of Sri Lanka, Ph.D. thesis, Gothenburg University, Gothenburg, Sweden. , 2003.

Zandbergen, P. A. and Barbeau, S. J.: Positional Accuracy of Assisted GPS Data from HighSensitivity GPSenabled Mobile Phones, Journal of Navigation, 64, 381399, https://doi.org/10.1017/S0373463311000051, 2011.

Zanutta, A., Lambertini, A., and Vittuari, L.: UAV Photogrammetry and Ground Surveys as a Mapping Tool for Quickly Monitoring Shoreline and Beach Changes, Journal of Marine Science and Engineering, 8, 52, https://doi.org/10.3390/jmse8010052, 2020.